Infragravity-wave modulation of short-wave celerity in the surf zone

Marion Tissier, Philippe Bonneton, Hervé Michallet, B. Gerben Ruessink

AGU PUBLICATIONS

JGR

Journal of Geophysical Research: Oceans

RESEARCH ARTICLE

10.1002/2015JC010708

Infragravity-wave modulation of short-wave celerity in the surf zone

M. Tissier[1], P. Bonneton[2], H. Michallet[3], and B. G. Ruessink[4]

[1]Environmental Fluid Mechanics Section, Delft University of Technology, Delft, Netherlands, [2]UMR 5805 EPOC CNRS, University of Bordeaux, Talence, France, [3]LEGI UMR 5519, University of Grenoble, Grenoble, France, [4]Department of Physical Geography, Faculty of Geosciences, Utrecht University, Utrecht, Netherlands

Key Points:
- Individual wave celerity is analyzed using high-resolution laboratory data
- A large intrawave variability in celerity is observed in the inner surf zone
- This variability is largely controlled by the infragravity waves

Correspondence to:
M. Tissier,
m.f.s.tissier@tudelft.nl

Citation:
Tissier, M., P. Bonneton, H. Michallet, and B. G. Ruessink (2015), Infragravity-wave modulation of short-wave celerity in the surf zone, *J. Geophys. Res. Oceans*, *120*, 6799–6814, doi:10.1002/2015JC010708.

Received 8 JAN 2015
Accepted 11 SEP 2015
Accepted article online 21 SEP 2015
Published online 20 OCT 2015

Abstract The cross-shore evolution of individual wave celerity is investigated using two high-resolution laboratory experiments on bichromatic waves. Individual waves are tracked during their onshore propagation and their characteristics, including celerity, are estimated. The intrawave variability in celerity is low in the shoaling zone but increases strongly after breaking. It is maximum when the infragravity-wave height to water depth ratio is the largest, that is to say close to the shoreline. There the observed range of individual wave celerity can be as large as the mean celerity value. This variability can be largely explained by the variations in water depth and velocity induced by the infragravity waves. The differences in celerity are such that they lead to the merging of the waves in the inner surf zone for most of the wave conditions considered. Again, the location at which the first waves start merging strongly correlates with the infragravity-wave height to water depth ratio. The consequences of these findings for celerity-based depth-inversion techniques are finally discussed. Surprisingly, accounting for the infragravity-wave modulation of the velocity field in the celerity estimate does not significantly improve depth estimation in the surf zone. However, it is shown that the occurrence of bore merging decreases significantly the coherence of the wavefield in the surf zone. This loss of coherence could hamper celerity estimation from pixel intensity time series and explain, at least partly, the relatively poor performance of depth-inversion techniques in the inner surf zone.

1. Introduction

In the last decade, remote-sensing-based methods have become increasingly popular to monitor coastal evolution [e.g., *Holman and Stanley*, 2007]. These methods often rely on the estimation of an average wave celerity from spatially coherent, instantaneous (∼1 Hz) time series of pixel intensity, which is used as a proxy to retrieve water depth [e.g., *Stockdon and Holman*, 2000; *Yoo et al*., 2011; *Almar et al*., 2008; *Holman et al*., 2013]. This so-called depth-inversion is an interesting alternative to in situ bathymetric surveys, as it, when repeated with time, provides an estimate of bathymetric change over large areas at relatively low cost; however, its accuracy depends crucially on the functional relationship between time-averaged wave celerity and water depth, that is to say on the choice of the parametrization for the celerity [see *Catalán and Haller*, 2008, for a review]. Wave celerity is also a key parameter for wave-propagation models. *Svendsen et al*. [2003] have shown for instance that an accurate estimation of celerity in phase-averaged models was essential for driving nearshore circulation. A parametrization of the broken-wave celerity is also often needed in phase-resolving Boussinesq models to compute the energy dissipation in the roller [e.g., *Schäffer et al*., 1993; *Madsen et al*., 1997]. Again, the choice of parametrization is critical [*Madsen et al*., 1997].

In practice, linear wave theory is often used to describe wave celerity, both in remote-sensing applications and in wave models. The celerity given by linear theory, estimated as

$$c_{lin} = \sqrt{\frac{g}{k}\tanh\left(k\bar{h}\right)}, \tag{1}$$

with k the local wave number, $\bar{h}$ the mean water depth, and g the gravitational acceleration, gives a good first-order estimation of wave celerity in the nearshore; however, linear theory generally underpredicts celerity in the last stages of shoaling and in the surf zone [e.g., *Suhayda and Pettigrew*, 1977; *Svendsen*

et al., 1978; *Stive*, 1980; *Thornton and Guza*, 1982]. Accounting for the mean currents in the linear dispersion relation does not significantly improve celerity prediction in the surf zone, as their magnitude in the direction of wave propagation is generally small when compared to the wave celerity [*Thornton and Guza*, 1982].

Several studies have shown that the errors given by linear theory were increasing with the relative wave height, defined as the wave height to water depth ratio [e.g., *Thornton and Guza*, 1982]. This behavior is called amplitude-dispersion in analogy with the linear frequency-dispersion, as, for a given water depth, the largest waves were seen to propagate faster than the smaller ones. Most efforts to improve the prediction of wave celerity have focused on this nonlinear effect. Taking into account the wave height through the use of nonlinear celerity models indeed leads to improved predictions and reduces depth estimation errors in the last stages of shoaling and in the surf zone [*Grilli*, 1998; *Catalán and Haller*, 2008; *Yoo et al*., 2011]; however, relatively large discrepancies between time-averaged measured and nonlinearly predicted celerities still remain in the inner surf zone [*Tissier et al*., 2011].

To further investigate these discrepancies, we focus in this paper on the infragravity waves. In the inner surf zone, the energy at infragravity frequencies (0.005–0.05 Hz under natural conditions) can exceed the energy contained at short-wave frequencies [e.g., *Guza and Thornton*, 1982; *Ruessink et al*., 1998]. Because of the local variations of water depth and velocity they induce, infragravity waves can modify short-wave characteristics, such as their amplitude and their wavelength [*Abdelrahman and Thornton*, 1987], and are expected to modify wave celerity. This effect on short-wave celerity is expected to be large in the inner surf zone, as infragravity-wave heights can be a large fraction of the mean water depth, and infragravity orbital velocities, which are experienced as a slowly varying-current by the short waves, a significant fraction of the short-wave celerity [e.g., *Haller and Özkan-Haller*, 2007].

Thornton and Guza [1982] suggested that the presence of infragravity waves could actually explain part of the mismatch between measured celerity spectra and linear theory in the surf zone. More specifically, they hypothesized that the convergence of the short waves on the infragravity-wave crest could lead to an increase of the apparent celerity, as these short waves benefit from a larger water depth and are convected by an onshore-directed current. It is therefore feasible that intrawave celerity variability affects the bulk estimate (average over many waves) and hence depth-inversion.

The influence of infragravity waves on individual short-wave celerity was disregarded in previous celerity studies which were generally based on the analysis of bulk estimates of the celerity. Besides, the few studies analyzing individual wave celerity have usually focused on periodic waves in the laboratory [e.g., *Stive*, 1980, 1984; *Svendsen et al*., 1978], for which the variability is minimal. The intrawave variability of celerity, however, can be large in a natural surf zone, as is illustrated by bore merging in the field (i.e., faster bores overtaking slower ones and merging, thereby reducing the number of waves). *Sénéchal et al*. [2001] have shown that bore merging could modify the wavefield considerably, with the observation of wave periods larger than twice the offshore mean period in the inner surf zone. The occurrence of bore merging, and the associated decrease in the number of waves, could hamper the celerity estimation from pixel intensity time series, as it relies on the spatial coherence of the signal.

In this paper, we aim at improving our understanding of individual short-wave celerity with a specific focus on the effect of infragravity waves on its variability in the surf zone. Our study is based on two laboratory experiments with bichromatic waves for which high-resolution (synchronized) time series of free-surface elevation are available. The resulting data set consists of free-surface and velocity measurements for two different beach slopes and a large range of short-wave and infragravity-wave characteristics. It will allow us to investigate both the effects of infragravity-wave transformation on short-wave celerity and the occurrence of bore merging. The paper is organized as follows. In section 2, we introduce the laboratory data sets as well as the methodology developed to characterize individual waves and their celerity. In section 3, we analyze our individual celerity data and focus more particularly on the influence of infragravity waves on short-wave propagation. This analysis will be completed with numerical experiments in section 4.1 to investigate how the type of infragravity-wave pattern (standing or progressive) influences bore merging. In section 4.2, we discuss the role of amplitude-dispersion on the observed variability in celerity. The consequences of our findings for depth-inversion methods are discussed in section 4.3. Our main conclusions are drawn in section 5.

2. Methods

2.1. Laboratory Data

This study analyzes two data sets collected during separate small-scale laboratory experiments. It focuses more specifically on the analysis of bichromatic wave cases, as the regular wave groups allow for the detailed study of short-wave and infragravity-wave interaction. The main characteristics of these experiments are presented below. Further details concerning the experimental setup can be found in *Ruessink et al*. [2013] and *van Noorloos* [2003].

2.1.1. GLOBEX Experiment

The GLOBEX laboratory experiment was conducted in the 110 m long Scheldegoot flume at Deltares (Delft, Netherlands) to investigate short-wave and infragravity-wave interaction over a very low-sloping (1:80) beach [*Ruessink et al*., 2013].

Eight wave conditions were considered in this experiment, out of which three were bichromatic. They were repeated 10 times with identical paddle motion for different instrument positions, resulting in a total of 190 measurement locations for the free-surface elevation η and 43 for the cross-shore velocity u. The waves were generated with a piston-type wave maker equipped with Active Reflection Compensation to minimize reflections from the wave paddle. The cross-shore spacing of the free-surface elevation measurements, dx, typically ranged between 0.55 and 0.74 m in the shoaling zone, and was 0.37 m in the surf and swash zones. The velocity measurements were performed with a spacing of 1.10 and 1.5 m at the upper beach, and 1.65 m at the lower beach. The free-surface and velocity time series were both recorded with a sampling frequency $F_s = 128$ Hz.

A strong infragravity-wave dissipation was observed in very shallow water during these experiments, resulting in mostly progressive infragravity-wave patterns. A detailed analysis of the underlying dissipation mechanisms for the irregular wave conditions can be found in *de Bakker et al*. [2015]. The present paper focuses on the three bichromatic wave conditions, which characteristics are shown in Table 1 (G1–G3). The primary frequencies f_1 and f_2 were multiple of the difference frequency $|f_1 - f_2|$, allowing for ensemble averaging over the wave groups. This part of the data is therefore particularly well suited for the detailed study of wave celerity since this procedure yields to more robust statistics. Moreover, the numerous measurements of flow velocity in the surf zone allow for a detailed study of the effects of the infragravity-wave current on celerity.

During the GLOBEX bichromatic experiments, some transverse or cross-mode waves were visually observed in the surf zone. These spurious waves were likely generated close to the breakpoint through resonance mechanism at a depth where the transverse mode-1 seiching can be excited at frequency $f_{res} = (f_1 + f_2)$ [*Michallet et al*., 2014]. As $f_{res} \propto |f_1 - f_2|$, these oscillations were not averaged out by the ensemble-averaging procedure. These cross-mode waves are expected to have negligible effect on the free-surface elevation measurements, as they exhibit an elevation node at the center of the flume, i.e., close to the location where the instruments were deployed; however, they generate secondary circulations and, as such, modify the mean horizontal velocity field [see *Michallet et al*., 2014, Figure 6].

Table 1. Wave Conditions for GLOBEX (G1-3) and *van Noorloos* [2003]'s (A1-4 and B1-4) Experiments[a]

Series	a_1 (m)	a_2 (m)	f_1 (Hz)	f_2 (Hz)	S	d_0 (m)
G1	0.09	0.01	6/15	7/15	1/80	0.85
G2	0.09	0.01	0.42	0.462	1/80	0.85
G3	0.07	0.03	0.42	0.462	1/80	0.85
A1	0.06	0.012	0.6714	0.4761	1/35	0.7
A2	0.06	0.012	0.6470	0.5005	1/35	0.7
A3	0.06	0.012	0.6348	0.5127	1/35	0.7
A4	0.06	0.012	0.6226	0.5249	1/35	0.7
B1	0.06	0.018	0.6470	0.5005	1/35	0.7
B2	0.06	0.024	0.6470	0.5005	1/35	0.7
B3	0.06	0.030	0.6470	0.5005	1/35	0.7
B4	0.06	0.036	0.6470	0.5005	1/35	0.7

[a] a_1 and a_2 (f_1 and f_2) are the primary amplitudes (frequencies) of the bichromatic incoming waves. S is the slope of the laboratory beach and d_0 the offshore water depth.

2.1.2. Van Noorloos' Experiment

The second experiment considered in this study was performed in the 40 m Long Research Flume at Delft University of Technology [*van Noorloos*, 2003; *van Dongeren et al*., 2007]. Different wave conditions were run 8 times over a 1:35 impermeable beach. This resulted in 80 measurement locations for free-surface elevation per condition with $F_s = 25$ Hz. The distance separating two consecutive measurements was 0.5 m in the shoaling zone and 0.3 m in the surf zone. Flow velocity was measured at four locations only ($F_s = 25$ Hz), three of them in the shoaling zone, and one close to the mean breakpoint.

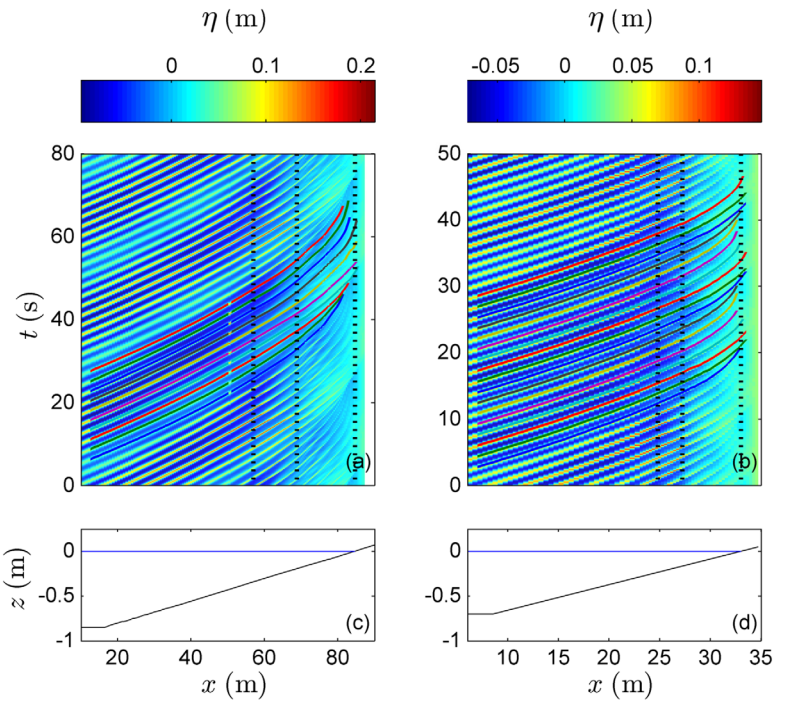

Figure 1. Space-time diagram of free-surface elevation, η, measured for (left) G3 and (right) A4 (see Table 1). The colored lines are the wave crest trajectories used to compute celerity. The vertical dashed lines show (from left to right) the position where the largest waves start breaking, the position where the smallest waves start breaking, and the location of the still waterline. (bottom) The bed profiles for both experiments ($x = 0$ at the wave maker, $z = 0$ at the still water level).

Table 1 describes the characteristics of eight bichromatic cases run during this experiment. For the A-series, the primary frequencies were varied to change the infragravity-wave frequency, while the amplitudes a_1 and a_2 were kept constant. The B-series correspond to an increasing amplitude modulation of the incoming waves, starting from wave condition A2.

This data set has a smaller temporal resolution than the GLOBEX data and only sparse measurements of flow velocity, but it includes a much larger range of offshore wave characteristics. In particular, these conditions correspond to different infragravity-wave reflection rate at the shoreline [see *van Dongeren et al.*, 2007], resulting in the development of progressive to quasi-standing infragravity waves. No ensemble averaging was performed for this data set, as the primary frequencies of the incoming bichromatic waves were not a multiple of the difference frequency.

2.2. Computation of Individual Wave Celerity

For a (quasi-)linear wavefield, individual wave celerity can be unequivocally defined for each harmonic as the phase velocity (equation (1)). Defining (individual) wave celerity for a nonlinear wavefield is not as straightforward. In the surf zone, nonlinearity generally prevails over frequency-dispersion [e.g., *Thornton and Guza*, 1982], and, therefore, the calculation of celerity per harmonic may not be the most relevant approach. Moreover, the waveshape can evolve quickly. As a result, different characteristic points of the wave can propagate at different speeds. Here we define wave celerity as the propagation speed of the individual crests. This is expected to have little impact for the inner surf zone, as the different characteristic points of a broken-wave travel at the same speed [*Stive*, 1980]; however, it should be kept in mind while analyzing data close to the breakpoint, as, due to its steepening, the wave crest propagates faster than other characteristic points, such as the trough.

To define this celerity, the time series of free-surface elevation were first combined in a time-space diagram (see examples in Figure 1). The waves belonging to N groups ($N = 1$ for the ensemble-averaged GLOBEX data, $N = 3$ otherwise) were identified at the most offshore locations and tracked during their propagation shoreward, resulting in the definition of individual wave trajectories. The individual wave celerity, c_i, was then calculated as the slope of the resulting trajectories.

The wave-tracking procedure is explained below. The crest at the location $x_{k+1}=x_k+dx$ was identified as the maximum of the free-surface elevation time series $\eta(x_{k+1},t)$ over the segment defined by $t_k+\delta t_{\min} < t < t_k+\delta t_{\max}$, where t_k is the arrival time of the crest at the preceding location x_k. $\delta t_{\min}$ and $\delta t_{\max}$ are estimates of the minimum and maximum durations needed for the crest to travel the distance dx. Their calculation was based on the assumption that the wave celerity c_i is between $0.4(g\bar{h})^{1/2}$ and $2.5(g\bar{h})^{1/2}$, with $\bar{h}$ the water depth averaged over the entire time series. The procedure was stopped when the algorithm failed to identify the crest at the next location. This often happened close to the shoreline, when the crest elevations approached zero, or just before merging, when two successive crests could not be distinguished by the algorithm anymore. When possible, the trajectories were manually extended to the still water line. The procedure results in trajectories of variable length, as shown by the colored lines in Figure 1.

To determine the slope of the trajectories at a given location, a linear regression was performed over the measurement points included in the interval of length $\Delta x=\alpha L$, with $\alpha > 0$ and L the local short-wave length. The choice of α for each data set depends mainly on its spatial resolution. Ideally, α should be much less than 1; however, to allow for reliable results, a sufficient number of points n should be used per regression. This is a limiting factor at the shallowest location, where the wavelength is smallest. For the GLOBEX data, we chose $\alpha=0.9$, resulting in a number of points typically between 3 and 15 for the linear regressions (nine points on average). For the Van Noorloos' data, α was set to 1.4 ($3 \leq n \leq 11$, average value of 8).

2.3. Estimation of Individual Wave Characteristics

A set of wave characteristics was then calculated for each crest identified during the tracking process. For each wave and at each location, the wave trough was defined as the first local minimum of free-surface elevation preceding the crest after applying a $T_0/5$-moving average to the time series ($T_0=\frac{2}{f_1+f_2}$). The wave height H_i was then computed as the difference of free-surface elevation between the crest and the trough.

The computation of the wave period and local water depth in which the waves propagate requires the decomposition of the time series into individual waves. Traditionally, a zero-crossing analysis is applied after filtering the free-surface elevation signal to remove the low-frequency fluctuations induced by the infragravity waves [e.g., *Hamm and Peronnard*, 1997]. However, our data set includes highly nonlinear data in shallow water in which there is not always a clear frequency separation between short and infragravity waves. Filtering out the low-frequency part of the signal could therefore alter heights and periods of the individual waves, as illustrated in *Power et al.* [2010] for field data. An alternative approach is thus adopted here. Individual waves were defined between two consecutive crests. The wave period, T_i, was calculated as the time separating these crests. The local water depth, h_i, was taken as the mean water depth over the wave period. As pointed out by *Power et al.* [2010], it would be more intuitive to define the waves based on their trough locations. This methodology was considered for our study, but consequently dismissed. It led to much noisier results when looking at the cross-shore evolution of the wave period and local water depth, because the relatively flat wave troughs could not be identified as precisely as the sharp wave crests.

Finally, the velocity time series (when available) were averaged over the individual waves, resulting in local estimates of the current U_i. These current estimates are of importance, as they can modify the propagation speed of the waves. *Kirby and Chen* [1989] have shown that in presence of a vertically variable current $U(z)$ such as $|U/c| < O(1)$, the waves were conveyed at the speed $U_e=\frac{1}{h}\int_{-\bar{h}}^{0} U(z)dz$ in shallow water. U_i was decomposed into two parts, a time-averaged current $\bar{u}$, due to the undertow and the cross-mode wave-induced circulation (GLOBEX data), and a slowly varying component, u_i, induced by the infragravity-wave orbital velocities. As the infragravity waves are in the shallow water regime, their orbital motion is assumed vertically constant, and u_i is representative of the depth-averaged velocity. On the other hand, $\bar{u}$ is expected to vary strongly along the vertical making the estimation of the depth-averaged velocity from a single measurement point rather difficult. As we are primarily interested in the intrawave variability of celerity, we decided to neglect the contribution of $\bar{u}$ and to assume that waves are mainly convected by the orbital velocity of the long waves ($U_e \approx u_i$). The absolute celerity, c_a, relative to the beach, can be therefore expressed as

$$c_a=c_r+u_i, \tag{2}$$

where c_r is a relative celerity estimate given by linear theory for instance.

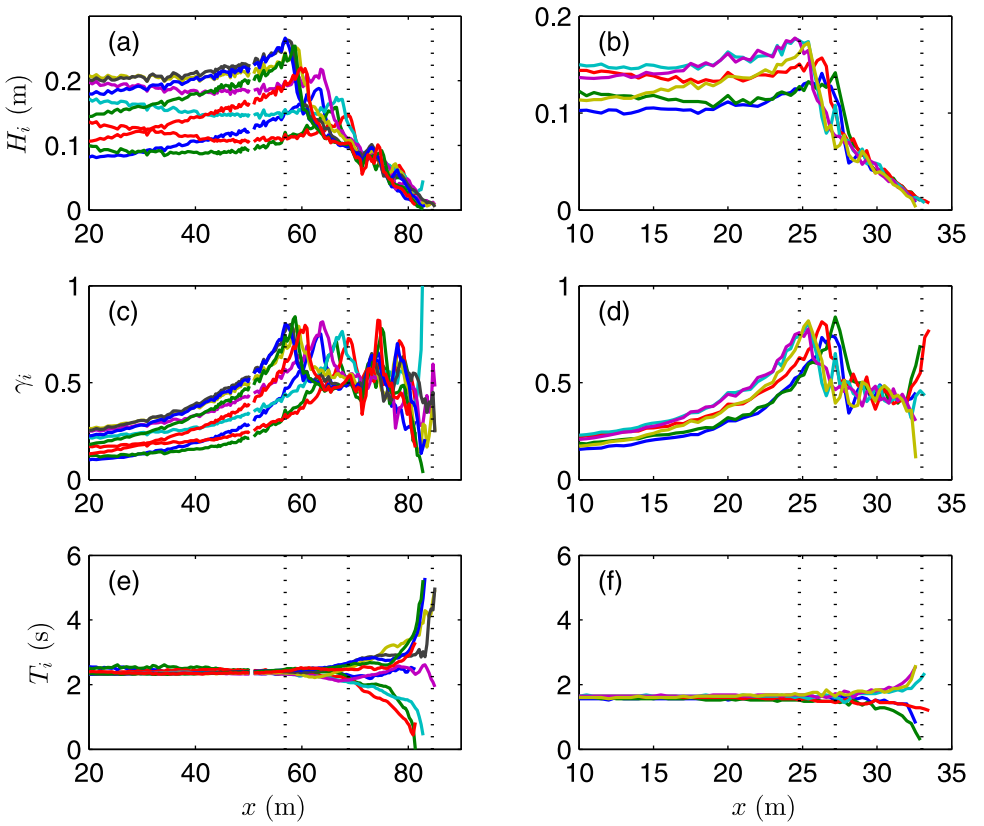

Figure 2. Cross-shore evolution of the (a, b) individual wave height H_i, (c, d) relative wave height γ_i, and (e, f) wave period T_i for (left column) G3 and (right column) A4. Each colored line corresponds to an individual wave. For clarity purposes, only the waves belonging to one wave group are provided for A4. The vertical dashed lines show (from left to right) the position where the largest waves start breaking, the position where the smallest waves start breaking, and the location of the still waterline.

2.4. Breakpoint Location and Normalized Water Depth

Following *Svendsen and Veeramony* [2001], the main breakpoint location, $x_{b,i}$, was defined for each wave as the first maximum of the relative wave height $\gamma_i = H_i/h_i$. Based on its location with respect to this breakpoint, each wave was then classified as nonbreaking or breaking/broken. A mean breakpoint location, x_b, was defined for each experiment as the average of the individual breakpoint locations. To allow comparing the various data sets, a normalized water depth d^* was defined as $d^* = d/d_b$, where d is the still water depth and $d_b = d(x = x_b)$. With this definition, $d^* = 1$ at the mean breakpoint, and $d^* = 0$ at the still water line.

3. Results

3.1. General Characteristics of the Individual Waves

The wave height, period, and relative wave height are shown in Figure 2 for cases G3 (left) and A4 (right). As expected from the offshore wave characteristics given in Table 1, a larger range of H_i can be seen at the most offshore locations for G3 than for A4 (Figures 2a and 2b). The range of H_i decreases strongly in the surf zone as the waves become depth-limited. A local H_i increase is observed for G3 at $x \approx 75$ m. It corresponds to the visual observation made during the experiment of a quasi-termination of breaking at $x \approx 70$ m followed by a quick reformation of the breaker (for all waves in G1 and G2, only for the smallest ones in G3). This phenomenon is specific to the GLOBEX bichromatic data and may be related to the development of the cross-waves mentioned earlier.

The relative wave height, $\gamma_i = H_i/h_i$, which characterizes locally the nonlinearity of the wavefield, is shown in Figures 2c and 2d. The first maximum amounts to 0.75–0.85 in both cases. For case G3, γ_i first decreases to a value of about 0.4, typical of the inner surf zone, but scatters substantially further onshore. In particular, a peak of γ_i is observed at about $x \approx 75$ m in the surf zone, with an amplitude similar to the one observed at the main breakpoint. This supports the idea of a local cessation of breaking. For the Van Noorloos'

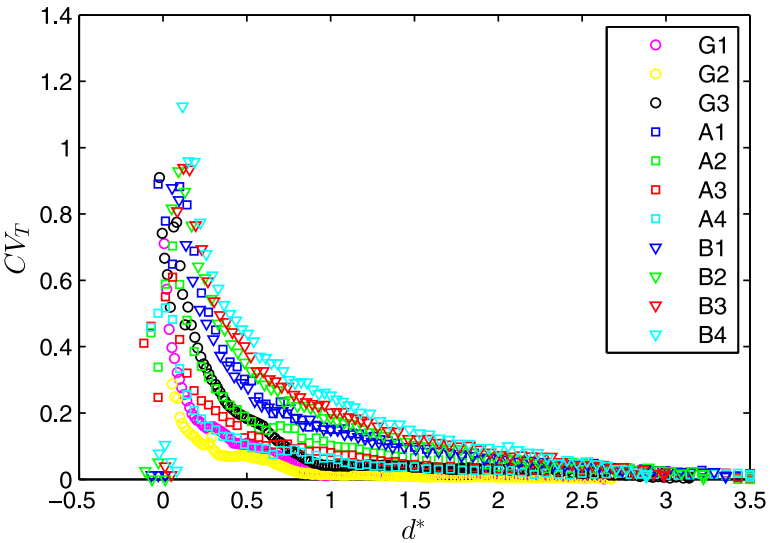

Figure 3. Normalized variability in T_i, CV_T, see equation (3), as a function of normalized depth d^* for the 11 wave conditions.

experiments, a more classical cross-shore evolution of the relative wave height is observed shoreward of the breakpoints, with a quasi-constant value of about 0.45 (see Figure 2d). The variability in γ_i increases again close to the shoreline.

Finally, Figures 2e and 2f show the evolution of the individual wave periods. Before breaking, there is little intrawave variability. The periods start differing when the waves enter the surf zone, suggesting an increased variability in celerity after the (main) breakpoint. For G3, some of the periods drop to zero in the inner surf zone, indicating that the crest convergence ultimately results in the merging of two consecutive bores (see also the timestacks Figure 1a). Similar behavior is observed for case A4, but the periods diverge at a slower rate. To characterize the deviation from the offshore period, the following coefficient is defined at each location and for each experiment:

$$CV_T(x) = \frac{\sqrt{\frac{1}{n_w(x)}\sum_{i=1}^{n_w(x)} \left(T_i(x) - T_i(x_0)\right)^2}}{T_0}, \tag{3}$$

with $T_i(x)$ the period of the ith wave at position x, T_0 the mean offshore period (at position x_0), and $n_w(x)$ the number of waves identified with the tracking procedure at position x. Figure 3 shows CV_T as a function of the normalized water depth d^* for the 11 experiments. For all cases, CV_T increases shoreward and is maximum at the shoreline ($d^* \approx 0$). The largest growth rates are observed in the inner half of the surf zone ($d^* < 0.5$). The cross-shore modification of the wave period and the phenomenon of wave merging will be investigated in more detail in section 3.3.

3.2. Wave Celerity

Figures 4a and 4b show the cross-shore evolution of the individual wave celerity for cases G3 and A4. Before breaking, the celerity exhibits little variability, and follows closely the linear dispersion relation (black dots in Figures 4a and 4b). In the last stages of shoaling, the deviation from linear theory increases to ∼15%, but individual waves still propagate at similar speed.

In the outer surf zone, the intrawave variability of the celerity increases considerably. A peak in celerity is first observed at the onset of breaking, see, for instance, Figure 4a, $x \approx 59$ m, just onshore of the outer breakpoint. This is consistent with our definition of the celerity as the propagation speed of the crest, which is projected forward when breaking is initiated. The celerity increase at breaking is less clear for A4 (Figure 4b), and more generally for the Van Noorloos' data, due to the lower spatial resolution of the celerity estimates. In the most inner part of the surf zone, celerity differences become even more pronounced. Some waves propagate at a smaller speed than the linear prediction, while others propagate faster than $1.3(g\bar{h})^{1/2}$, an empirical modification of linear theory for surf zone waves [*Stive*, 1980]. For G3, the range in celerity ($\Delta c = c_{\max} - c_{\min}$) at the most

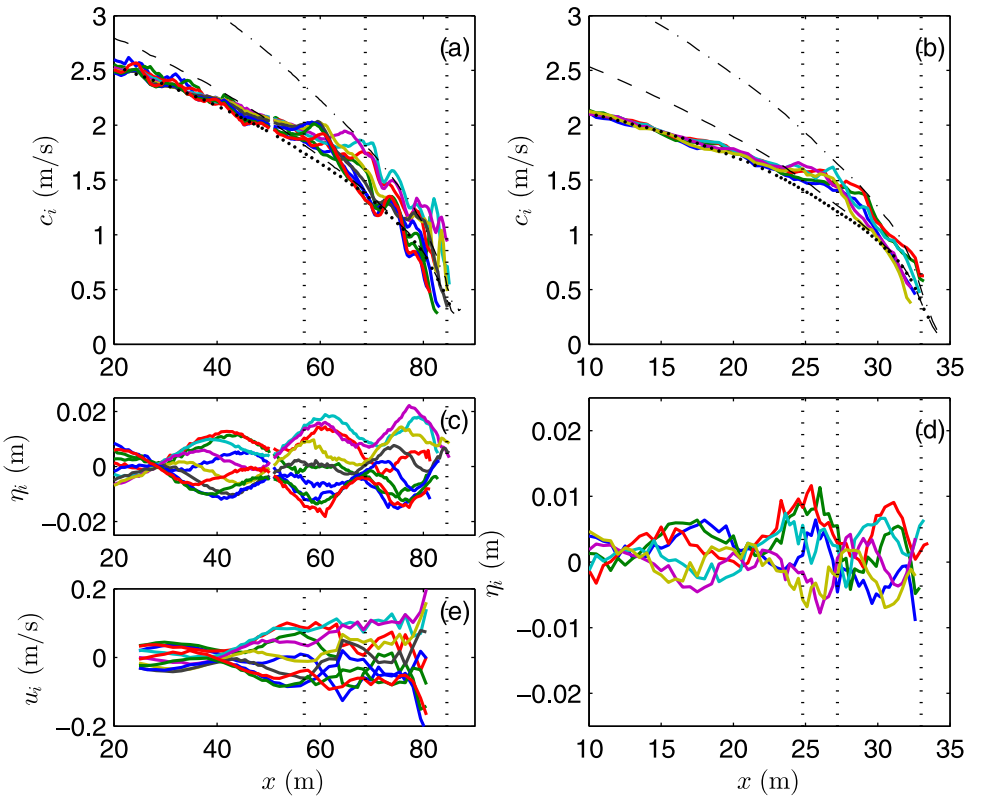

Figure 4. (a) Individual wave celerity, (c) infragravity-wave-induced variations of the water level η_i, and (e) velocity u_i ($u_i > 0$: onshore-directed current) for case G3. (b, d) Individual wave celerity and variations of water level for case A4 (too few velocity measurements for case A4). In Figures 4a and 4b, the black dots show linear celerity c_{lin} (equation (1)) calculated from the mean offshore period T_0 and the local mean water depth $\bar{h}$, the thin dashed line is $(g\bar{h})^{1/2}$ and the dash-dotted line is $1.3(g\bar{h})^{1/2}$. For a given case, each wave has a designated color (same colors as in Figure 2). See caption of Figure 1 for definition of the vertical dotted lines.

onshore locations is up to 120% of the mean celerity $\bar{c}$, while $\Delta c/\bar{c}$ is less than 10% before breaking. The variability in c is less for case A4, as expected from the cross-shore evolution of the periods in Figure 2c. For A4, $\Delta c/\bar{c}$ reaches a maximum of 75% close to the shore.

The individual wave celerities of the 11 wave experiments were then normalized as $c^* = c_i/c_{lin}$ (see equation (1), where k is calculated using the mean offshore period and the mean water depth). To investigate the importance of amplitude-dispersion for our data set, the normalized wave celerity is represented as a function of the relative wave height γ_i in Figure 5. Data were separated between nonbreaking (Figure 5a) and breaking or broken waves (Figure 5b) following the procedure introduced in section 2.4. For the nonbreaking waves, c^* increases with γ_i. As expected, c^* is close to 1 at the beginning of shoaling ($\gamma_i \approx 0.1$, Figure 5a); it increases to about 1.2 in the last stages of shoaling ($\gamma_i \approx 0.8$), with little scatter in the observations. This suggests that amplitude effects explain most of the deviations from linear theory before breaking.

Even though c^* still broadly increases with γ_i for surf zone waves (see bin-averaged values Figure 5b), there is obviously much more scatter. The standard deviations (vertical bars in Figure 5) are largest for $\gamma_i \approx 0.3-0.5$, typical values for inner surf zone waves. As shown in Figure 5b (colors), the outlying observations usually correspond to locations where the infragravity-wave height to water depth ratio is large ($H_{rms,lf}/\bar{h} \gtrsim 0.25$; $H_{rms,lf}$ was estimated as $\sqrt{8m_0}$, where m_0 is the zeroth-order moment calculated for frequencies less than half the main primary frequency). When the standard deviation of c^* is plotted as a function of the mean value of $H_{rms,lf}/\bar{h}$ for each class, an approximately linear trend is obtained (Figure 6). This suggests that infragravity waves affect the intrawave variability in celerity considerably, when their height, and therefore the variations of water depth they induce, is large enough with respect to the mean water depth ($\gtrsim$0.15).

Infragravity waves do influence celerity not only through the variations of elevation they induce but also through the associated changes in the velocity field. The variations of the water depth ($\eta_i = h_i - \bar{h}$) and

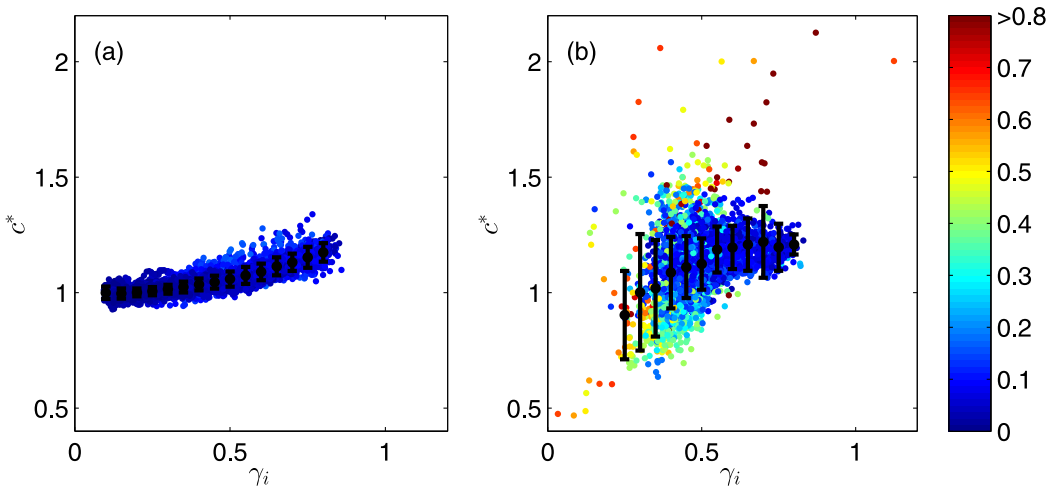

Figure 5. Normalized celerity $c^*=c_i/c_{lin}$ as a function of the relative wave height $\gamma_i=H_i/h_i$ for the 11 wave experiments. (a) Shoaling wave celerity only (6119 celerity estimates) and (b) breaking and broken waves only (3346 estimates). The data are divided into bins based on the value of γ_i (γ_i between 0.05 and 1.5, with a step of 0.05). The black dots are mean c^* values for these data bins (only the bins where $n \geq 10$ are shown). The error bars are ± 1 standard deviations per bins. The colors of the scatterplot indicate the value of the root-mean-square infragravity-wave height to water depth ratio $H_{rms,If}/\bar{h}$ at the location where the celerity were measured.

velocity ($u_i=U_i-\bar{u}$) induced by the infragravity waves for each tracked short wave of G3 are shown in Figures 4c and 4e. A well-developed nodal structure can be observed at the most offshore locations, $x \lesssim 50$ m. As expected for a standing wave, the nodes in elevation correspond to antinodes in velocity (e.g., $x \approx 28$ m, Figures 4c and 4e). In the surf zone, the infragravity waves exhibit a more progressive pattern, with less-defined antinodes and nodes. The fastest waves in the surf zone propagate in the largest water depths and benefit from an onshore infragravity-wave-induced current (e.g., cyan line in Figures 4a, 4c, and 4e). In other words, they are riding on the infragravity-wave crest. On the other hand, the slowest waves propagate in the smallest depth, and are slowed down by an opposing infragravity-wave current ($u_i < 0$) as they propagate in the trough of the infragravity wave (e.g., red line in Figures 4a, 4c, and 4e).

To quantify the respective importance of the low-frequency variations of u and h on surf zone celerity, the observations are compared to the celerity predicted by linear theory using the mean water depth $\bar{h}$ (Figure 7a), the local water depth h_i (Figure 7b), and finally the local water depth with an additional correction to account for the effects of the infragravity-wave-induced current u_i (Figure 7c, see also equation (2)). Figure 7 is based on a reduced data set, including only surf zone observations for which velocity measurements were available (G1, G2, and G3). As amplitude effects are not accounted for in the celerity predictors, they globally underestimate celerity. The role of amplitude-dispersion for our data set will be discussed in more detail in section 4.2. To quantify the differences between the three celerity estimates, the relative error between measured (c_i) and estimated (c_{pred}) celerity is defined as

$$R_{rms}=\sqrt{\frac{1}{N}\sum_{j=1}^{N}\left(\frac{c_{pred,j}-c_{i,j}}{c_{i,j}}\right)}, \tag{4}$$

where N is the number of waves. When considering the full data set (black and gray dots in Figure 7, $mean(H_{rms,If}/\bar{h})=0.08$), the differences in R_{rms} are small: 13.3% for $c_{pred}=(g\bar{h})^{1/2}$, 12.4% for $c_{pred}=(gh_i)^{1/2}$, and 12.0% for $c_{pred}=(gh_i)^{1/2}+u_i$. Accounting for the low-frequency variations of water level and velocity significantly decreases the scatter at the shallowest water depths. For $\bar{h} \leq 0.10$ m, which corresponds to data in the most onshore third of the surf zone, $R_{rms}=19.0\%$ when the celerity prediction is calculated using the mean water depth, 16.5% with a local depth estimate, and 13.9% when the low-frequency current is also accounted for (see gray dots in Figure 7, $mean(H_{rms,If}/\bar{h})=0.25$).

3.3. Crest Convergence

We have seen in section 3.1 that the variability in celerity resulted in the convergence of the wave crests in the surf zone (see time-space diagram in Figure 1 and the individual periods in Figures 2e and 2f). For this

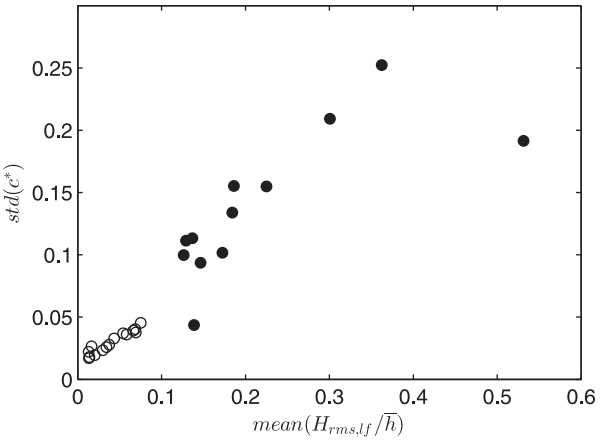

Figure 6. Standard deviation of c^* for each data bin defined in Figure 5 as a function of the averaged $H_{rms,lf}/\bar{h}$ for the same bin. The circles correspond to nonbreaking waves and the filled circles to breaking or broken waves.

convergence to happen, some waves need to consistently travel faster than others for a sufficient duration. In other words, not only the difference in instantaneous celerity of the waves at a given location is important, but also its variation through time. As the intrawave variability of celerity is largely determined by the infragravity waves, it is of interest to understand how the short waves propagate with respect to the infragravity waves in shallow water.

Outside the surf zone, incoming infragravity waves are bound and propagate at the group speed, which is, in deep and intermediate water depth, significantly less than the phase celerity at which the short waves propagate. This changes in the surf zone, as infragravity waves are released (for an analysis, see *de Bakker et al.* [2013]), and travel with the shallow water phase celerity $(g\bar{h})^{1/2}$ (dashed line in Figures 4a and 4b). In the shallow water surf zone, both short-wave and infragravity-wave celerities are therefore relatively close. This means that waves located on the crest of the incident infragravity waves in the outer part of the surf zone are likely to stay on the positive part of the incoming infragravity wave while propagating through the surf zone.

In case of a predominantly onshore progressive infragravity wave in the surf zone, the waves riding on the infragravity-wave crest benefit simultaneously from a maximum u_i and η_i during their propagation through the surf zone (e.g., Figures 4c and 4e). The situation is more complex for cases involving a more standing infragravity pattern in the surf zone. In that case, the water depth in which the waves propagate is strongly modulated by the outgoing infragravity waves. As a result, the water depth experienced by the waves riding on the incoming infragravity-wave crest oscillates between a maximal positive value at the antinodes, and about zero at the nodes (e.g., Figure 4d). u_i is expected to follow the same pattern but with a phase lag of 45°, i.e., it will be maximum positive at the nodes and zero at the antinodes. On the other hand, waves on the incoming infragravity-wave trough will propagate in such a way that $\eta_i \leq 0$ and $u_i \leq 0$. This explains qualitatively why, even in a standing case, individual wave celerities can consistently differ in the surf zone, making wave convergence possible. Wave propagation over progressive and standing infragravity waves will be discussed more extensively using numerical experiments in section 4.1.

Figure 8a shows the normalized depth where the first waves start merging, $d^*_{merging}$, for each experiment as a function of the relative infragravity-wave height $H_{rms,lf}/\bar{h}$ at the mean breakpoint ($d^*=1$). For the smallest values of $H_{rms,lf}/\bar{h}$, bore merging started in the swash zone ($d^*_{merging} \leq 0$ for G1) or even did not occur (G2). For the other experiments, waves start merging in the inner surf zone ($0 < d^* < 0.5$). $d^*_{merging}$ increases linearly with the infragravity relative wave height ($r = 0.91$). The strength of the correlation

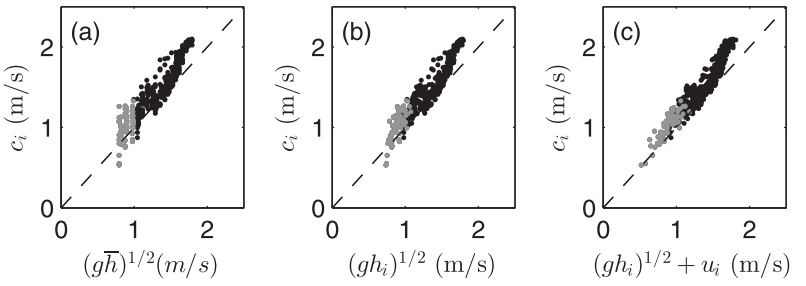

Figure 7. Individual wave celerity c_i in the surf zone as a function of (a) $(g\bar{h})^{1/2}$, (b) $(gh_i)^{1/2}$, and (c) $(gh_i)^{1/2}+u_i$. Only data for which velocity measurements were available are shown (391 estimates). The gray dots correspond to shallowest water depth ($\bar{h} < 0.10$ m, i.e., $d^* \leq 1/3$).

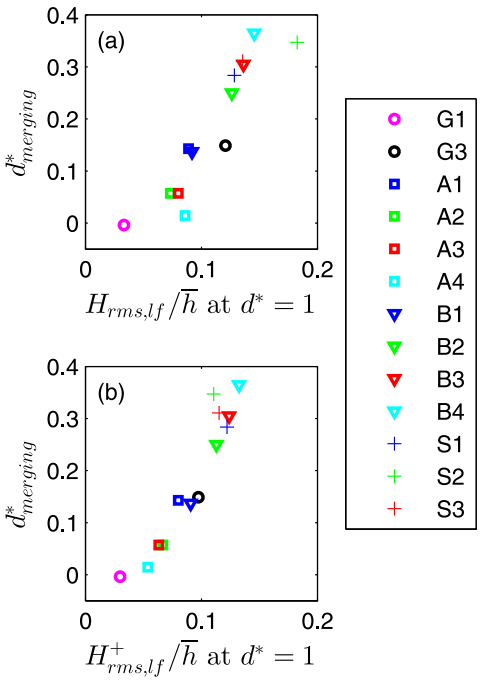

Figure 8. Normalized position at which the waves start merging $d^*_{merging}$ as a function of the root-mean-square infragravity-wave height to water depth ratio for the (a) total and (b) incoming infragravity signal. The bold symbols are the experimental data. The crosses are numerical results discussed in section 4.1. No merging was identified for G2.

increases ($r = 0.97$) when $d^*_{merging}$ is shown as a function of $H^+_{rms,lf}/\overline{h}$, where $H^+_{rms,lf}$ is the incoming infragravity-wave height calculated following the separation method of *van Dongeren et al.* [2007] (see Figure 8b).

4. Discussion

4.1. Occurrence of Bore Merging

To further investigate how the infragravity-wave pattern affects short-wave convergence in the surf zone, several numerical simulations were carried out with the phase-resolving model SWASH [*Zijlema et al.*, 2011]. SWASH is based on the nonlinear shallow water equations including nonhydrostatic effects and has been extensively validated for the propagation of short and infragravity waves from the shoaling to the swash zone using the Van Noorloos' data set [*Rijnsdorp et al.*, 2014].

The numerical model was run with the same offshore wave characteristics as case B2, but for different bed profiles. More precisely, the offshore bathymetry was kept the same, but the foreshore slope was changed at $x = 31$ m, i.e., 2 m seaward of the still water line. Simulations were performed with a foreshore slope of 1:10, 1:20, and 1:35 (see bed profiles in Figure 9d). These run are called S1, S2, and S3 in the following. The third run is used as a reference simulation, as it can be compared with the experimental case B2. For all three simulations, SWASH was run with two vertical layers; wave breaking was handled using the parametrization introduced in *Smit et al.* [2013]. A quadratic friction term was used. The friction coefficient was based on the Manning-Strickler formulation, which writes $c_f = 0.015(d_r/h)^{1/3}$, with d_r the apparent roughness value. Following *Rijnsdorp et al.* [2014], we chose $d_r = 0.0075$ m. The grid resolution and time step were set to 0.01 m and 0.002 s, respectively. The simulations were run for 10 min. Only the last 5 min (after steady state was observed) were used for analysis.

Figure 9 compares the short-wave and infragravity-wave root-mean-square heights for the three simulations. While the short-wave heights are similar, the infragravity-wave characteristics differ (Figure 9a). In S1 and S2, partly standing/progressive infragravity-wave patterns developed, while a mainly progressive pattern developed for S3, in fair agreement with the experimental data (see symbols in Figure 9a). The cross-shore evolution of the incoming and outgoing infragravity-wave heights, calculated using the decomposition method of *van Dongeren et al.* [2007], are shown in Figures 9b and 9c. The differences in the total infragravity-wave height can be explained by the different reflection rate at the shoreline, and, therefore, by the intensity of the outgoing infragravity-wave signal. At $x \approx 30$ m, the reflection rate, calculated as the outgoing to incoming infragravity-wave flux ratio, is 0.79 for S1, 0.20 for S2, and 0.01 for S3.

Figure 10 quantifies the evolution of the short-wave period for the three model outputs. Offshore of the point where the slope was changed (vertical dotted line at $d^* = 0.27$), the crests are converging at the same rate. Therefore, the type of infragravity-wave pattern does not seem to be relevant to explain the convergence rate of the crests. This is consistent with Figure 8b, which showed a stronger correlation between the location where wave merging initiates and the relative infragravity-wave height when only the incoming infragravity wave was considered. The numerical datapoints (crosses in Figure 8) follow the same trend, and get closer to each other when $H^+_{rms,lf}$ is used instead of $H_{rms,lf}$.

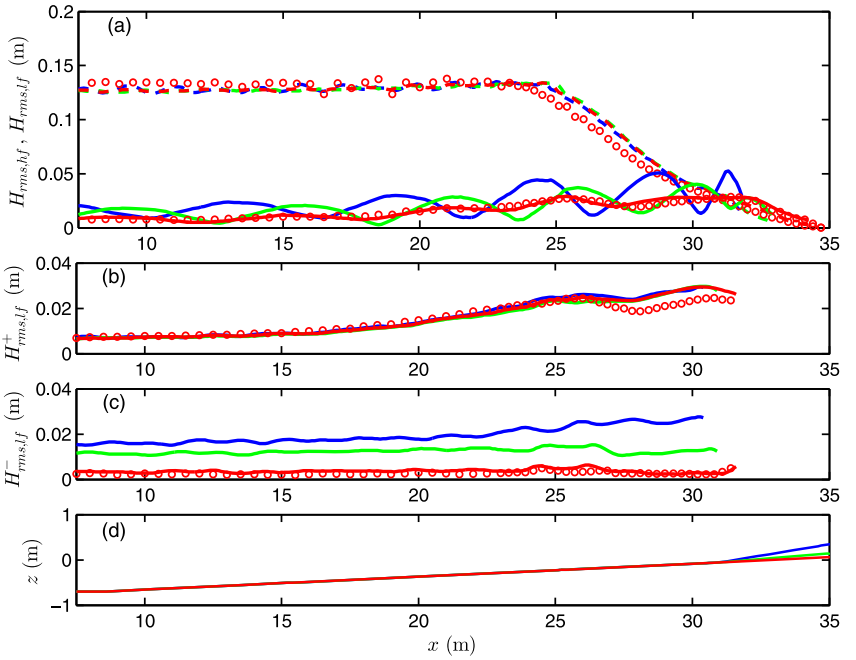

Figure 9. Short-wave and infragravity-wave heights for the three simulations. (a) Root-mean-square wave heights for the short waves ($f > f_1/2$, dashed lines), and for the infragravity-waves (solid lines). (b, c) The incoming and outgoing infragravity root-mean-square heights. (d) The cross-shore bed profiles. The blue lines correspond to the 1:10 slope (S1), the green lines to the 1:20 slope (S2), and the red lines correspond to the 1:35 slope (S3). The red circles in Figures 9a–9c are the laboratory data for B2.

4.2. Amplitude-Dispersion

Several studies have observed a positive correlation between short-wave envelope and infragravity waves in the surf zone [e.g., *Guza et al.*, 1984; *Abdelrahman and Thornton*, 1987]. In such a case, short waves propagating on the infragravity-wave crest would not only benefit from a higher water depth and a following current, but would also tend to have a higher wave height than the waves propagating on the trough. Amplitude-dispersion could therefore increase the infragravity-wave modulation of short-wave celerity in the surf zone. In this section, we investigate the importance of amplitude-dispersion for our data set.

The correlation coefficient $R_{\eta_{lf},|A|}$ between the short-wave envelope $|A(t)|$ and the infragravity-wave $\eta_{ig}(t)$ is calculated at each cross-shore location. The short-wave envelope is defined as [*Janssen et al.*, 2003]:

$$|A(t)| = |\eta_{hf}(t) + i\Gamma\{\eta_{hf}\}|_{lf}, \tag{5}$$

where $\Gamma\{\cdot\}$ denotes the Hilbert transform operator, and the subscript *hf* (*lf*) indicates high-pass (low-pass) filtering of the time series. For our data sets, $R_{\eta_{lf},|A|}$ is mostly positive in the surf zone, although some null or even negative values are observed for the GLOBEX cases at the locations where breaking was observed to stop temporarily. At $d^*_{merging}$ (location where waves start merging), the correlation coefficient is positive for all our experiments. It varies between 0.22 and 0.69, with an average value of 0.46. This confirms that amplitude effects could enhance the intrawave variability in celerity in the inner surf zone.

To further quantify this effect, the individual wave celerity c_i was compared to several celerity predictors accounting for the wave height [*Svendsen et al.*, 1978; *Booij*, 1981; *Bonneton*, 2004]. As in Figure 7, we limit our analysis to surf zone data where velocity estimates were available. The results given by the two most accurate predictors (lowest R_{rms} for our data set) are described below. These are the classical bore model introduced by *Svendsen et al.* [1978]

$$c_{bore} = \sqrt{\frac{g h_c h_t (h_c + h_t)}{2h^2}}, \tag{6}$$

and the empirically derived predictor introduced by *Booij* [1981]

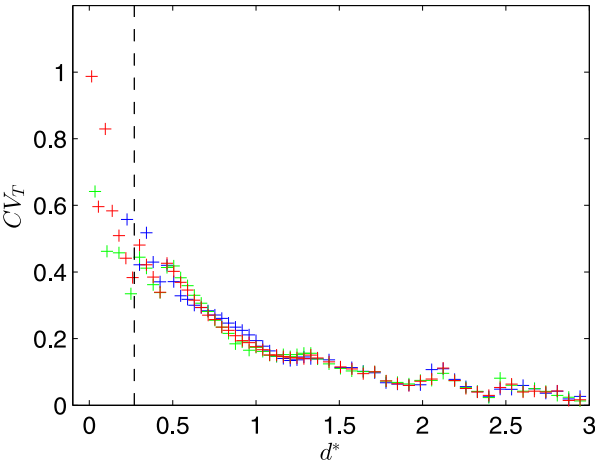

Figure 10. Normalized variability in wave period CV_T as a function of normalized depth d^* for the numerical experiments S1 (blue), S2 (green), and S3 (red). The vertical dashed line is the location at which the bed slope was changed ($x = 31$ m).

$$c_{booij} = \sqrt{\frac{g}{k}\tanh\left(k(h+\frac{H}{2})\right)}, \qquad (7)$$

where h_c and h_t are the depths at the wave crest and trough, H is the wave height ($H = h_c - h_t$), h the water depth, and k the wave number. Here we take $h = h_i$ and $H = H_i$, and k is estimated for $T = T_i$. Figure 11 compares the celerity data to the model predictions when infragravity-wave-induced currents are accounted for. As expected, accounting for amplitude-dispersion improves the overall agreement. For the full data set (black and gray dots in Figure 11), $R_{rms} = 7.3\%$ for $c_{pred} = c_{booij} + u_i$, and 9.6% for $c_{pred} = c_{bore} + u_i$.

The largest deviations between c_i and $c_{bore} + u_i$ are observed for the highest celerity values (outer surf zone). This is expected as *Svendsen et al.*'s [1978] model was derived based on the analogy between surf zone waves and fully developed bores. In the most inner third of the surf zone (gray dots), both models perform comparably, with $R_{rms} = 8.5\%$ for Svendsen's bore model, and $R_{rms} = 9.4\%$ for Booij's model when the infragravity-wave-induced current u_i is accounted for. Again, not accounting for the infragravity-wave-induced modulation of the current decreases the agreement at the shallowest locations considerably ($R_{rms} = 12.7$ and 13.5% for Svendsen's and Booij's models, respectively). This confirms the importance of the infragravity-wave modulation to describe the variability in individual wave celerity.

4.3. Consequences for Depth-Inversion

We have seen that the very large intrawave variability in the surf zone can, to a large extent, be related to the influence of the infragravity waves. In this subsection, we discuss the consequences of these observations for depth-inversion. We focus here on case G3, for which a strong underlying infragravity-wave signal was measured, and where the variability in celerity was of the same order of magnitude as the mean celerity at the most onshore locations.

Estimates $\tilde{h}_i$ of the local water depth were computed from the individual wave celerity and period using the linear dispersion relationship and were then averaged. Depth estimates were also computed from bulk celerity numbers obtained with a simple time domain cross-correlation method. In this method, 2 min long time series (five wave groups) distant from $\delta x \approx 0.9L$ were cross-correlated to determine the time-lag δt separating the arrival of the wave trains from one position to the next. The bulk celerity was calculated as $c_{Xcor} = \delta x / \delta t$. The depth $\tilde{h}_{Xcor}$ was then computed based on c_{Xcor} and the mean period $\bar{T}$ at the considered location. Surprisingly, few differences can be observed between depth estimated from individual celerities and the one computed from the bulk celerity, except at the shallowest location, just offshore of the first merging point. Both give a root-mean-square error of about 5.4 cm when compared to the measured mean water depth in the surf zone. Accounting from the infragravity-wave current, i.e., calculating depth estimates from $c_i - u_i$ instead of c_i, decreases the scatter of the individual depth estimates but gives very similar values after averaging. These results show that accounting for the intrawave variability in celerity does

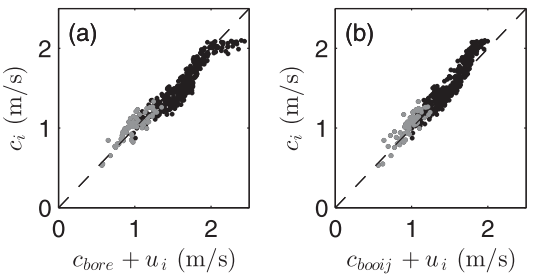

Figure 11. Individual wave celerity c_i in the surf zone as a function of (a) $c_{bore} + u_i$ and (b) $c_{booij} + u_i$. Only data for which velocity measurements were available are shown (391 estimates, same data points as Figure 7). The gray dots correspond to shallowest water depth ($\bar{h} < 0.10$ m, i.e., $d^* \lesssim 1/3$).

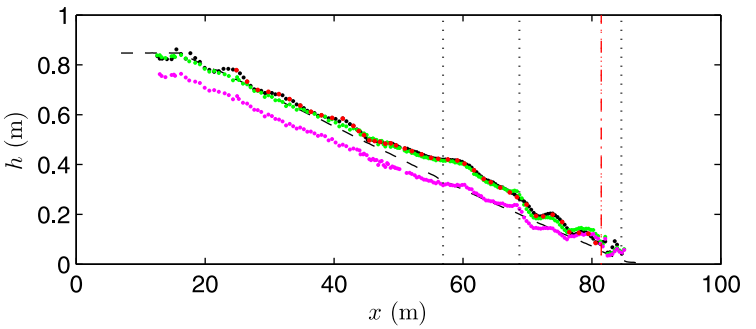

Figure 12. Depth estimates (dots) and measured water depth (dashed line) for case G3. Black dots: average of the individual water depths $\bar{h}_i$, where $\tilde{h}_i$ is calculated based on linear theory from c_i and T_i. Red dots: same calculation, but accounting for the infragravity-wave current, i.e., $\tilde{h}_i$ calculated from $c_i - u_i$. Green dots: depth calculated from c_{Xcor} and $\bar{T}$ using linear theory. Magenta dots: depth estimated from c_{Xcor}, $\bar{T}$ and $\bar{H}$ using Booij's celerity predictor (equation (7)). The red dash-dotted line indicates the position where waves start merging. See caption of Figure 1 for definition of the vertical dotted lines.

not significantly improve depth-prediction in the surf zone. For depth-inversion purposes, the use of a bulk celerity number seems therefore sufficient.

For comparison, a second depth estimate was calculated from c_{Xcor} using a nonlinear celerity predictor. Booij's model (equation (7)) was chosen, as it was identified by *Catalán and Haller* [2008] as one of the most efficient nonlinear celerity predictors for depth-inversion. For this depth computation, we use the averaged periods and wave heights, both calculated from the individual wave characteristics and the current is not accounted for (see magenta dots in Figure 12). While this estimate performs poorly in the shoaling zone, it gives a root-mean-square depth error of 2.3 cm in the surf zone, which is significantly less than the errors obtained when using linear theory. Thus, while the intrawave variability in celerity is mainly controlled by the infragravity waves, the deviation of the averaged celerity estimates from linear theory is induced primarily by amplitude effects.

Thornton and Guza [1982] suggested that part of the discrepancies between celerity observations in the surf zone and linear theory could be explained by the convergence of the short waves on the infragravity-wave crests. This would explain that a series of waves in the inner surf zone propagates, in average, faster than expected as they locally experience a larger water depth than the averaged depth $\bar{h}$ calculated from the entire time series. It would lead to an overestimation of the depth, even if a perfectly accurate celerity predictor was used. To quantify the importance of this phenomenon for our data set, the mean water depth

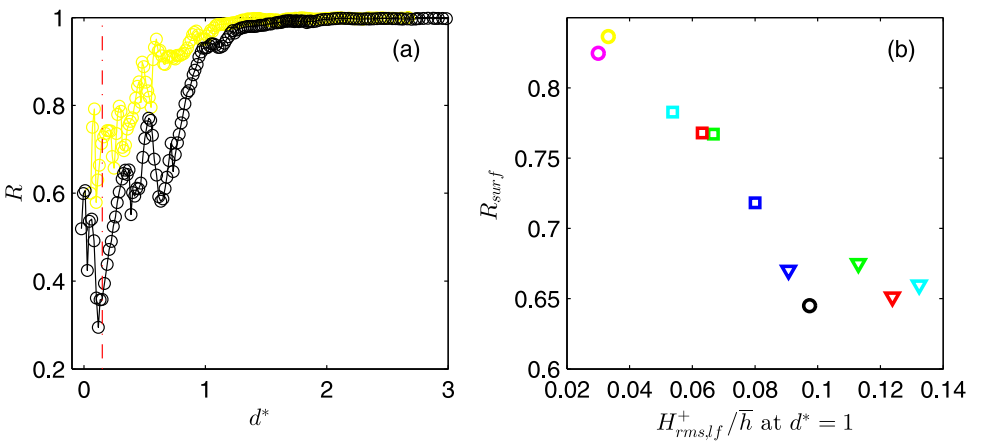

Figure 13. (a) Maximum correlation coefficient R between surface elevation time series separated by a cross-shore distance $\delta x \approx 0.9L$ as a function of normalized depth d^* for G2 (yellow) and G3 (black). The red dash-dotted line indicates $d^*_{merging}$ for G3 (no wave merging in G2). (b) Averaged correlation coefficient over the surf zone ($d^* \leq 1$) as a function of the incoming infragravity-wave height to depth ratio at $d^* = 1$. See Figure 3 for legend (colors).

actually experienced by the short waves $\overline{h_i}=\frac{1}{n_w}\sum_{i=1}^{n_w} h_i$, which is the best possible depth estimate, is compared to the actual water depth $\bar{h}$. As long as no waves have merged ($d^* \geq 0.15$), $\overline{h_i}=\bar{h}$ (see definition of h_i in section 2.3). After merging, the relative amount of waves on the infragravity-wave crests increases. The relative difference between $\overline{h_i}$ and $\bar{h}$ increases then to 16% when 4 out of 10 waves are left in the group ($d^* \approx 0.06$), and to about 30% when only 3 waves remain at the shore ($d^* \approx 0.04$). Similar behavior can be observed for the other experimental cases once waves start merging.

To summarize, it appears that as long as no (or only few) waves have merged, the variability in celerity has only limited influence on the accuracy of depth-inversion methods based on bulk celerity estimates. This variability, however, is responsible for the convergence of waves, which can result in significant modifications of the wavefield. This is expected to decrease the spatial coherence of the wave signal, and, as a result, to hamper the quality of celerity estimates which are used to retrieve the water depth [e.g., see *Holman et al*., 2013]. Figure 13 shows the cross-shore evolution of the maximum correlation coefficient R between the time series used for the computation of c_{Xcor} for cases G2 and G3. In both cases, the correlation decreases when the waves start breaking. However, the loss of coherence occurs at a faster rate for G3, which is also the case where the wave convergence was the strongest (see Figure 3). Similar observations can be made for the other experimental cases. In general, the lowest values of R are observed at the points where merging occurs. This is confirmed in Figure 13b, which shows that the correlation coefficient averaged over the surf zone strongly decreases with increasing infragravity-wave height to depth ratio. Thus, poor performance in shallow water could be due, in part, to the loss of coherence in short-wavefield.

5. Conclusions

In this paper, the propagation of individual waves in the surf zone was analyzed based on two sets of high-resolution laboratory experiments. For all 11 analyzed bichromatic cases, the intrawave variability in celerity increases when waves enter the surf zone. This variability is seen to relate to the infragravity-wave height to water depth ratio and is therefore maximum in the inner surf zone, where it can be of the same order of magnitude as the mean celerity. The variability in celerity is such that it leads to the merging of the waves in the inner surf zone for 9 out of the 11 cases considered. The position at which bore-bore capturing processes start is shown to correlate with the incoming infragravity-wave height to water depth ratio at the breakpoint ($r = 0.97$).

The discrepancies between individual wave celerities and linear theory in the inner surf zone can be significantly decreased when accounting for both the modulation of water level and velocity induced by the infragravity waves. Using these corrected celerity estimates to calculate water depth does not significantly improve the predictions compared to depth-inversion based on bulk celerity estimates. Thus, the use of bulk celerity estimates seems sufficient with regard to depth-inversion. Knowledge of the individual wave celerity remains of importance as its variability can lead to large spatial modifications of the wavefield, decreasing the coherence of the wave signal in the cross-shore and hampering the estimation of celerity in the inner part of surf zone.

Acknowledgments
The GLOBEX project was supported by the European Community's Seventh Framework Program through the grant to the budget of the Integrated Infrastructure Initiative Hydralab IV (contract 261520). The authors thank all researchers and Deltares staff members involved in this project. The authors also thank A. van Dongeren and J. van Noorloos for kindly providing their experimental data, as well as D. Rijnsdorp for his advices regarding SWASH. The data are freely available from the first author upon request (m.f.s.tissier@tudelft.nl).
B. G. Ruessink was funded by the Netherlands Organisation for Scientific Research (NWO) (contract 821.01.012). Additional funding was provided by the CNRS-INSU LEFE-MANU program through the SOLi project.

References

Abdelrahman, S. M., and E. B. Thornton (1987), Changes in the short wave amplitude and wave-number due to infragravity waves, in *Coastal Hydrodynamics Conference*, edited by R. A. Dalrymple, 809 pp., Am. Soc. of Civ. Eng., N. Y.
Almar, R., P. Bonneton, N. Sénéchal, and J. A. Roelvink (2008), Wave celerity from video imaging: A new method, in *Proceedings of the 31st International Conference on Coastal Engineering*, edited by J. M. Smith, pp. 661–673, Am. Soc. of Civ. Eng., Hamburg, Germany.
Bonneton, P. (2004), Wave celerity in the surf zone, in *Proceedings of the 29th International Conference on Coastal Engineering*, vol. 1, pp. 392–401, Am. Soc. of Civ. Eng., Lisbon, Portugal.
Booij, N. (1981), Gravity waves on water with non-uniform depth and current, PhD thesis, Delft Univ. of Technol., Delft, Netherlands.
Catalán, P. A., and M. C. Haller (2008), Remote sensing of breaking wave phase speeds with application to non-linear depth inversions, *Coastal Eng.*, *55*(1), 93–111.
de Bakker, A., M. Tissier, V. Marieu, N. Sénéchal, A. Ruju, J. Lara, and G. Ruessink (2013), Infragravity wave propagation and dissipation on a low-sloping laboratory beach, in *Proceedings of the Conference on Coastal Dynamics*, pp. 443–452, Arcachon, France.
de Bakker, A. T. M., T. H. C. Herbers, P. B. Smit, M. F. S. Tissier, and B. G. Ruessink (2015), Nonlinear infragravity-wave interactions on a gently sloping laboratory beach, *J. Phys. Oceanogr.*, *45*, 589–605, doi:10.1175/JPO-D-14-0186.1.
Grilli, S. T. (1998), Depth inversion in shallow water based on nonlinear properties of shoaling periodic waves, *Coastal Eng.*, *35*, 185–209.
Guza, R. T., and E. B. Thornton (1982), Swash oscillations on a natural beach, *J. Geophys. Res.*, *87*(C1), 483–491.
Guza, R. T., E. B. Thornton, and R. A. Holman (1984), Swash on steep and shallow beaches, in *Proceedings of 19th Conference on Coastal Engineering*, pp. 708–723, Am. Soc. of Civ. Eng., Houston, Tex.

Haller, M. C., and H. T. Özkan-Haller (2007), Waves on unsteady currents, *Phys. Fluids*, *19*(12), 126–601, doi:10.1063/1.2803349.
Hamm, L., and C. Peronnard (1997), Wave parameters in the nearshore: A clarification, *Coastal Eng.*, *32*(23), 119–135, doi:10.1016/S0378-3839(97)81746-2.
Holman, R., N. Plant, and T. Holland (2013), cBathy: A robust algorithm for estimating nearshore bathymetry, *J. Geophys. Res. Oceans*, *118*, 2595–2609, doi:10.1002/jgrc.20199.
Holman, R. A., and J. Stanley (2007), The history and technical capabilities of Argus, *Coastal Eng.*, *54*(67), 477–491, doi:10.1016/j.coastaleng.2007.01.003.
Janssen, T. T., J. A. Battjes, and A. R. van Dongeren (2003), Long waves induced by short-wave groups over a sloping bottom, *J. Geophys. Res.*, *108*(C8), 3252, doi:10.1029/2002JC001515.
Kirby, J. T., and T.-M. Chen (1989), Surface waves on vertically sheared flows: Approximate dispersion relations, *J. Geophys. Res.*, *94*(C1), 1013–1027.
Madsen, P. A., O. R. Sørensen, and H. A. Schäffer (1997), Surf zone dynamics simulated by a Boussinesq type model. Part I. Model description and cross-shore motion of regular waves, *Coastal Eng.*, *32*(4), 255–287.
Michallet, H., et al. (2014), GLOBEX: Wave dynamics on a shallow sloping beach, in *Proceedings of the HYDRALAB IV Joint User Meeting*, Lisbon.
Power, H. E., M. G. Hughes, T. Aagaard, and T. E. Baldock (2010), Nearshore wave height variation in unsaturated surf, *J. Geophys. Res.*, *115*, C08030, doi:10.1029/2009JC005758.
Rijnsdorp, D. P., P. B. Smit, and M. Zijlema (2014), Non-hydrostatic modelling of infragravity waves under laboratory conditions, *Coastal Eng.*, *85*, 30–42, doi:10.1016/j.coastaleng.2013.11.011.
Ruessink, B. G., M. G. Kleinhans, and P. G. L. Van den Beukel (1998), Observations of swash under highly dissipative conditions, *J. Geophys. Res.*, *103*(C2), 3111–3118.
Ruessink, G., H. Michallet, P. Bonneton, D. Mouazé, J. L. Lara, P. A. Silva, and P. Wellens (2013), GLOBEX: Wave dynamics on a gently sloping laboratory beach, in *Proceedings of the Conference on Coastal Dynamics*, pp. 1351–1362, Arcachon, France.
Schäffer, H. A., P. A. Madsen, and R. Deigaard (1993), A Boussinesq model for waves breaking in shallow water, *Coastal Eng.*, *20*(3–4), 185–202.
Sénéchal, N., H. Dupuis, P. Bonneton, H. Howa, and R. Pedreros (2001), Observation of irregular wave transformation in the surf zone over a gently sloping sandy beach on the French Atlantic coastline, *Oceanol. Acta, 324*(6), 545–556.
Smit, P., M. Zijlema, and G. Stelling (2013), Depth-induced wave breaking in a non-hydrostatic, near-shore wave model, *Coastal Eng.*, *76*, 1–16, doi:10.1016/j.coastaleng.2013.01.008.
Stive, M. J. F. (1980), Velocity and pressure field in spilling breakers, in *Proceeding of the 17th International Conference on Coastal Engineering*, vol. 1, pp. 574–566, Am. Soc. of Civ. Eng., Sydney, N. S. W., Australia.
Stive, M. J. F. (1984), Energy dissipation in waves breaking on gentle slopes, *Coastal Eng.*, *8*(2), 99–127.
Stockdon, H. F., and R. A. Holman (2000), Estimation of wave phase speed and nearshore bathymetry from video imagery, *J. Geophys. Res.*, *105*(C9), 22,015–22,033, doi:10.1029/1999JC000124.
Suhayda, J. N., and N. R. Pettigrew (1977), Observations of wave height and wave celerity in the surf zone, *J. Geophys. Res.*, *82*(9), 1419–1424.
Svendsen, I., and J. Veeramony (2001), Wave breaking in wave groups, *J. Waterw. Port Coastal Ocean Eng.*, *127*(4), 200–212, doi:10.1061/(ASCE)0733-950X(2001)127:4(200).
Svendsen, I. A., P. A. Madsen, and J. B. Hansen (1978), Wave characteristics in the surf zone, in *Proceedings of the 16th Conference on Coastal Engineering*, pp. 520–539, Am. Soc. of Civ. Eng., Hamburg, Germany.
Svendsen, I. A., W. Qin, and B. A. Ebersole (2003), Modelling waves and currents at the {LSTF} and other laboratory facilities, *Coastal Eng.*, *50*(12), 19–45, doi:10.1016/S0378-3839(03)00077-2.
Thornton, E. B., and R. T. Guza (1982), Energy saturation and phase speeds measured on a natural beach, *J. Geophys. Res.*, *87*(C12), 9499–9508.
Tissier, M., P. Bonneton, R. Almar, B. Castelle, N. Bonneton, and A. Nahon (2011), Field measurements and non-linear prediction of wave celerity in the surf zone, *Eur. J. Mech. B Fluids*, *30*(6), 635–641.
van Dongeren, A. R., J. A. Battjes, T. T. Janssen, J. van Noorloos, K. Steenhauer, G. Steenbergen, and A. J. H. M. Reniers (2007), Shoaling and shoreline dissipation of low-frequency waves, *J. Geophys. Res.*, *112*, C02011, doi:10.1029/2006JC003701.
van Noorloos, J. C. (2003), Energy transfer between short wave groups and bound long waves on a plane slope, Master's thesis, Delft Univ. of Technol., Delft, Netherlands.
Yoo, J., H. Fritz, K. Haas, P. Work, and C. Barnes (2011), Depth inversion in the surf zone with inclusion of wave nonlinearity using video-derived celerity, *J. Waterw. Port Coastal Ocean Eng.*, *137*(2), 95–106, doi:10.1061/(ASCE)WW.1943-5460.0000068.
Zijlema, M., G. Stelling, and P. Smit (2011), SWASH: An operational public domain code for simulating wave fields and rapidly varied flows in coastal waters, *Coastal Eng.*, *58*(10), 992–1012, doi:10.1016/j.coastaleng.2011.05.015.